Available online at www.sciencedirect.com
SCIENCE DIRECT®
Journal of Magnetic Resonance 172 (2005) 268–278
JMR Journal of Magnetic Resonance
www.elsevier.com/locate/jmr

Increasing the sensitivity of 2D high-resolution NMR methods applied to quadrupolar nuclei

J.P. Amoureux[a,*], L. Delevoye[a], S. Steuernagel[b], Z. Gan[c], S. Ganapathy[d], L. Montagne[a]

[a] LCPS, CNRS-8012, ENSCL-USTL, 59652 Villeneuve d'Ascq, France
[b] Bruker-Biospin GMBH, 76287 Rheinstetten, Germany
[c] NHMFL, 32310 Tallahassee, Florida, USA
[d] NCL, 411 008 Pune, India

Received 4 June 2004; revised 31 October 2004
Available online 2 December 2004

Abstract

Gan and Kwak recently proposed a soft-pulse added mixing (SPAM) idea in the classical two-pulse multiple-quantum magic-angle spinning scheme. In the SPAM method, a soft $\pi/2$ pulse is added after the second hard-pulse (conversion pulse) and all coherence orders in between them are constructively used to obtain the signal. We, here, further extend this idea to distributed samples where the signal mainly results from echo pathways and that from anti-echo pathways dies out after a few t_1 increments. We show that, with a combination of SPAM and collection of fewer anti-echoes, an enhancement of the signal to noise ratio by a factor of ca. 3 may be obtained over the z-filtered version. This may prove to be useful even for samples with long T_2' relaxation times.

Keywords: Solid-State NMR; Quadrupolar nuclei; High-resolution; Sensitivity

1. Introduction

Nuclear magnetic resonance (NMR) of half-integer spin quadrupolar nuclei ($S = 3/2, 5/2, 7/2, 9/2$) was limited for a long period of time to the observation of one-dimensional (1D) magic-angle spinning (MAS) spectra. These spectra were not of high-resolution, as they remained broadened by the second-order quadrupolar interaction. The observation of quadrupolar nuclei with half-integer spin got a significant boost in 1995, when Frydman and Harwood introduced the two-dimensional (2D) multiple-quantum MAS (MQMAS) method that correlates a multiple-quantum coherence during the evolution time t_1 with the central transition (CT) during the observation time t_2 [1]. A complementary technique was proposed in 2000 when Gan introduced the 2D satellite-transition MAS (STMAS) method, which correlates the satellite transitions during t_1 with the CT during t_2 [2]. For all crystallite orientations, both methods refocus the second-order quadrupole dephasings along a unique axis according to: $t_2 = R(S) \cdot t_1$ [3], where the constant $R(S)$ depends on the spin quantum number S and the order of multiple-quantum coherence. This refocusing allows obtaining 2D frequency spectra from which the indirect dimension becomes, after shearing, an isotropic dimension (δ_{iso}), and the second dimension (δ_2) the classical MAS one [4–6]. The two methods are in fact complementary as their comparison allows deducing species that are submitted to motions or that are close to mobile nuclei (e.g., water molecules) [7]. This comparison has been facilitated recently by the introduction of a unified representation for both methods [8].

Since 1995, numerous developments have been introduced for MQMAS. They were first concerned with

* Corresponding author. Fax: +33 3 20 43 68 14.
E-mail address: jean-paul.amoureux@univ-lille1.fr (J.P. Amoureux).

1090-7807/$ - see front matter © 2004 Elsevier Inc. All rights reserved.
doi:10.1016/j.jmr.2004.11.001

getting pure absorption 2D spectra, and the proposed sequences fit into two categories of methods, namely, amplitude-modulated (AM) and phase-modulated (PM) data acquisition. The first category of sequences generally includes a z-filter part [9–12], whereas the second one is of full-echo type [13,14].

NMR, being an insensitive spectroscopy, often requires numerous accumulations, especially for 2D high-resolution methods applied to quadrupolar nuclei in solids. With respect to the first MQMAS sequence introduced by Frydman and Harwood [1], numerous improvements have been proposed to enhance the sensitivity of 2D MQMAS experiments. In MQMAS (and STMAS), the most frequently used sequences, such as z-filter or full-echo acquisition sequence, are composed of three pulses: two hard-pulses (HP_1 for the MQ creation and then, after t_1, HP_2 for the conversion) with rf-field amplitudes in the 50–250 kHz range, followed by one soft-pulse (SP) of amplitude in the 5–20 kHz range. While HPs can modify all coherence orders, SPs affect only those concerning the central transition. The excitation efficiency of HP_1, which is "naturally" large, has still been improved by using amplitude-modulated pulses before and after HP_1 [15]. However, most of the proposed improvements for sensitivity enhancement have mainly concerned HP_2. Initially, HP_2 was generated with a very brief (a few μs) strong continuous-wave (CW) irradiation [9–14]. For spins $S = 3/2$, it has been proposed to increase the pulse length to one-quarter of the rotor period to obtain a $\pm 3Q \leftrightarrow \pm 1Q$ rotational-induced adiabatic coherence transfer (RIACT) [16]. In the past few years, several authors have proposed different methods to replace HP_2 by a pulse frequency-modulated either discontinuously (FAM: fast amplitude modulated) [17] or continuously (DFS: double frequency sweep) [18]. Very recently, a long (3–4 rotor-periods) fast spinning transfer enhancement at rotary resonance (FASTER) CW conversion pulse has also been proposed in case of very fast MAS [19]. However, the improvements with these frequency-modulated or long pulses have been obtained at the expense of the robustness of the sequences. Indeed, the optimization of HP_2 in FAM or DFS requires fitting three parameters (rf-amplitude so that sweeping rate and range in DFS; pulse lengths, delays, and number of blocks in FAM), which may be time consuming in case of weak signals. This is much less the case when using short CW HP_2, where only its length must be optimized, the rf amplitude being most of the time at its maximum. In addition, it must be noted that a modern spectrometer is required for proper execution of DFS. FASTER conversion pulse uses weak rf-fields and is therefore very sensitive to off-resonance effects such as non-linear dephasing and attenuation. Its main applications may be for MQMAS of low gamma nuclei under very fast rotation or to reintroduce homonuclear dipolar interaction between quadrupolar nuclei [20]. In addition to these sensitivity enhancements related to coherence transfers in the MQMAS sequence itself, three additional main improvements have been proposed. The first one concerns the recycling of the observed signal through the use of multiple echoes (CPMG-MQMAS) [21], which leads to a large signal-to-noise (S/N) gain when the homogeneous transverse relaxation is much smaller than the inhomogeneous one [22]. The second one concerns the initial pre-saturation of all population levels with rotationally assisted FAM population transfer [17,23]. The last one concerns the rotor synchronization of the evolution time t_1 [24].

Very recently, two new improvements that concern the ensemble HP_2–SP have been proposed by Gan and Kwak [25]. Up to now, in all MQMAS or STMAS sequences, a single coherence level was being selected in between HP_2 and SP: $0Q$ in z-filter and $+1Q$ in full-echo experiments. The idea proposed by Gan and Kwak is to use all coherence levels in between HP_2 and SP in a constructive way. In fact, if one takes into account the SP weak rf-field and the large first-order quadrupolar dephasings that occur on even coherence levels, the final signal comes mainly from transfers through $0Q$ and $\pm 1Q$ levels after HP_2. The enhancement can be obtained in two ways. The first method uses the multiplex phase cycling [26] of HP_2 and SP to acquire MQMAS spectra from various coherence transfer pathways simultaneously. This addition of weighted spectra collected with no extra time enhanced the S/N by 64% on a model compound [25]. However, multiplex phase cycling requires additional data storage and modification of processing software. The second method, called soft pulse added mixing (SPAM), is based on a complete alias of coherence transfer pathways. It is simply an enhanced mixing of coherence orders and requires no additional data storage.

In this paper, we show theoretically and experimentally that the SPAM (ensemble HP_2–SP) concept leads to a doubling of the echo and anti-echo signals in MQMAS experiments. SPAM concept, with the echo/anti-echo acquisition method, can be incorporated easily into high-resolution 2D echo/anti-echo experiments leading to pure-phase spectra. For distributed samples, which show large resonances with only a few detectable anti-echoes in the indirect dimension, MQMAS may be performed by collecting echoes and a fewer number of anti-echoes than a conventional echo/anti-echo experiment without compromising on the quality of the pure-phase 2D spectral line-shapes. We utilize this to show that by incorporating SPAM in MQMAS, and by acquiring echoes and fewer anti-echoes, the S/N ratio may be enhanced by a factor of ca. 3 compared with the CW z-filter MQMAS experiment. This is possible as more signal averaging can be done because only few anti-echoes are collected. We then show the applicability

of this method in the detection of non-bridging oxygens of $3Al_2O_3$–$48.5Na_2O$–$48.5P_2O_5$ glasses, for a first experimental characterization of oxygens in PO–Al sites.

2. SPAM and echo signal in 3QMAS experiments

SPAM method, besides leading to a doubling of the echo signal, has a favorable property for MQMAS in that it performs with nearly the same efficiency the following transfers: $+3Q \rightarrow -1Q$, $-3Q \rightarrow -1Q$, and $+3Q \rightarrow +1Q$ [25]. FAM and DFS only do the latter two with high efficiency. Hence, while FAM and DFS are well suited to use in PM full-echo (or full-anti-echo) acquisition experiments, SPAM method is ideally suited for echo/anti-echo experiments.

SPAM method may be incorporated into the classical two-pulse, HP_1–HP_2, scheme or full-echo (or full-anti-echo) acquisition scheme. We denote the former as $SPAM_{E/AE}$ and the latter as $SPAM_{FE}$ (or $SPAM_{FAE}$) schemes, and they are depicted in Figs. 1A and C, respectively, along with the coherence orders selected for the echo pathway in 3QMAS experiments for $S > 3/2$ in Figs. 1B and D, respectively. In $SPAM_{E/AE}$ high-resolution 2D spectra of quadrupolar nuclei with half-integer spin, the signal intensity results mainly from the echo pathway. Indeed, the anti-echo signal then cancels after only a few t_1 slices and the corresponding 2D

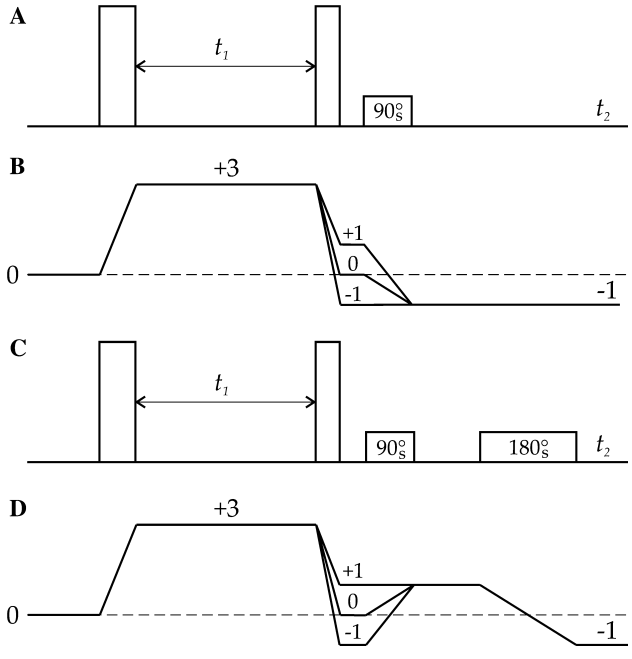

Fig. 1. Pulse sequences and coherence transfer pathways in SPAM 3QMAS experiments. (A) Pulse sequence for $SPAM_{E/AE}$ experiment and (B) its echo pathway for spin $S > 3/2$. (C) Pulse sequence for $SPAM_{FE}$ and $SPAM_{FAE}$ experiment, and (D) their echo ($S > 3/2$) or anti-echo ($S = 3/2$) pathway.

absorptive contribution is weak. The magnetization issuing from the anti-echo pathway is thus mainly used to minimize the dispersive parts that come from the echo pathway. The echo (or anti-echo: Eq. (3)) pathway for both these sequences for 3QMAS experiments may be explicitly written as:

$$\mathrm{SPAM_{E/AE}}: 0Q \rightarrow -3Q\,(t_1) \rightarrow_x \mathrm{all} \rightarrow_{-x} -1Q\,(t_2) \quad \text{if } S = 3/2, \tag{1}$$

$$\mathrm{SPAM_{E/AE}}: 0Q \rightarrow +3Q\,(t_1) \rightarrow_x \mathrm{all} \rightarrow_{x} -1Q\,(t_2) \quad \text{if } S > 3/2, \tag{2}$$

$$\mathrm{SPAM_{FAE}}: 0Q \rightarrow +3Q\,(t_1) \rightarrow_x \mathrm{all} \rightarrow_{-x} +1Q\,(\tau + Rt_1) \rightarrow -1Q\,(\tau + t_2) \quad \text{if } S = 3/2, \tag{3}$$

$$\mathrm{SPAM_{FE}}: 0Q \rightarrow +3Q\,(t_1) \rightarrow_x \mathrm{all} \rightarrow_{-x} +1Q\,(\tau) \rightarrow -1Q\,(\tau + Rt_1 + t_2) \quad \text{if } S > 3/2. \tag{4}$$

In the above, transfers related to HPs or SPs are indicated by $\rightarrow$ or $\rightarrow$, respectively. Another pathway: $0Q \rightarrow -3Q(t_1) \rightarrow +1Q(\tau) \rightarrow -1Q(\tau + Rt_1 + t_2)$ can also be used for $S = 3/2$ in the case of delayed acquisition. This pathway describes a full-echo signal, which means that a delay τ shorter than that corresponding to Eq. (3), which describes a full anti-echo signal, can be used. However, this pathway, which requires a coherence level jump of 4 for HP_2, is much less efficient than the one described in Eq. (3) that requires only a coherence level jump of 2.

The first pulse (HP_1) is phase cycled to select only the targeted coherence level for the echo pathway ($+3Q$ or $-3Q$) [27]. When using SPAM, its phase and that of the receiver are calculated by assuming a $0Q$ level between HP_2 and SP. Phases of HP_2 and SP are fixed to $\pm x$. They have the same or opposite signs according to whether the global transfer for SPAM is in between coherence levels of opposite or identical signs, respectively. The delay in between HP_2 and SP must be as short as possible to avoid dephasing of magnetizations not located on zero quantum level. Coherence level used during t_1 for the anti-echo pathway is symmetrical to the one used for the echo pathway. This implies a change of sign for SP in Fig. 1A to collect the anti-echo signal. It is therefore impossible to record simultaneously the echo and the anti-echo pathways in SPAM experiments [25]. It may be noted that the pulse sequence in Fig. 1A is the same as that for z-filter experiments where both the echo and the anti-echo pathways are collected simultaneously [12].

To quantify the maximum efficiency that can be obtained for the echo pathway with these methods, we carried out a systematic numerical analysis of the optimal transfer conditions. For five rf-field amplitudes (50, 100, 150, 200, and 300 kHz) for the HPs, we maximized the powder-averaged final CT intensity by varying

systematically the HP lengths (HP_1 and HP_2) as well as the amplitude and lengths of the SPs as a function of the quadrupole coupling constant: $C_Q = e^2qQ$. In order not to decrease the MQMAS efficiency with too fast a rotation [28], we have adopted a MAS speed just sufficient to eliminate sidebands. Irradiations were always done on-resonance and the Larmor frequency was fixed to $\nu_0 = 105$ MHz.

Optimal HP_1 lengths were always found to be identical for all sequences, with or without SPAM. They only depend on the spin value S, the C_Q value, the HP rf-field amplitude, and the spinning speed ν_R. HP_2 lengths corresponding to SPAM methods are optimal when the $3Q \rightarrow 0Q$ transfer is maximal, and thus, are identical to their optimal values in z-filter experiment [12].

For z-filter and SPAM methods, optimal values of the SP just following HP_2 are equal (z-filter) or close to 90°_s (SPAM). However, it must be noted that SPAM efficiency being proportional to $\sqrt{2} + \sin(\mathrm{SP})$ [25], its value is actually not critical as it varies smoothly versus the duration of SP and as an example is relatively equal to 0.6, 1, and 0.6 for SP = 0, 90°_s, and 180°_s, respectively. For full-echo acquisition experiments (with and without SPAM), the optimum last SP is always equal to 180°_s.

3. Spins-3/2

3.1. Echo sensitivity: simulations

In this section, we analyze the intensity of the signal for spins-3/2 corresponding to the following experiments: z-filter, $SPAM_{E/AE}$, full-anti-echo acquisition, and $SPAM_{FAE}$. CT values represented in Figs. 2, 3, 5, and 6 are normalized with respect to the signal that can be observed in 1D experiments after a 90°_s SP.

We first compare the echo sensitivity of z-filter and $SPAM_{E/AE}$ experiments as, apart from phase cycling, the corresponding pulse sequences are the same (Fig. 1A). The CT amplitude due to the echo pathway for both the experiments is plotted in Fig. 2 as a function of the quadrupole interaction strength. The curves present one maximum and the amplitude of the echo signal observed with SPAM ($SPAM_{E/AE}$ sequence) is more than doubled with a moderate rf-field amplitude of 100 kHz with respect to the z-filter sequence.

We now compare the echo sensitivity in full-anti-echo acquisition experiments with and without SPAM given in Fig. 3. When using one of these two sequences, a full-anti-echo is normally observed if the delay τ is sufficient. This full-anti-echo doubles the signal, but also increases simultaneously the noise by a factor of $\sqrt{2}$. To directly compare S/N ratios obtained in all experiments, CT values represented for full-echo and full-anti-echo experiments (Figs. 3 and 6) were multiplied by $\sqrt{2}$. However, a complete comparison of S/N ratios also

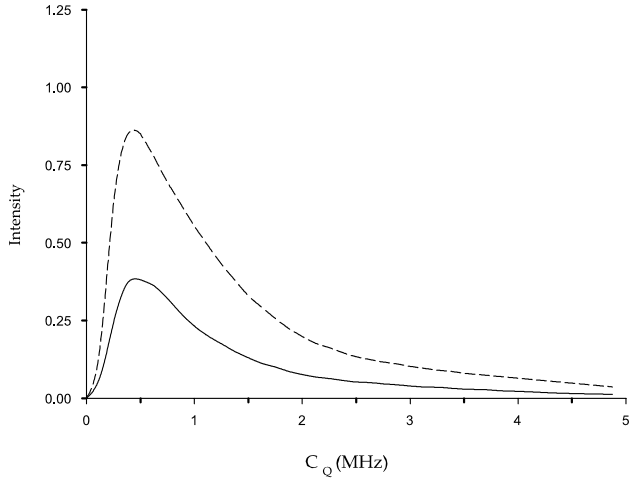

Fig. 2. $S = 3/2$: efficiency of the echo pathway in z-filter (continuous line: $0 \rightarrow -3 \rightarrow 0 \rightarrow -1$) and $SPAM_{E/AE}$ (dashed line: $0 \rightarrow -3 \rightarrow$ all $\rightarrow -1$) experiments as a function of C_Q (0–5 MHz), with $B_1(\mathrm{HP}) = 100$ kHz. $\eta_Q = 0$; $\nu_0 = 105$ MHz; $\nu_R = 10$ kHz ($C_Q <$ 3 MHz), $\nu_R = 15$ kHz ($C_Q > 3$ MHz); and $B_1(\mathrm{SP}) = 5$ kHz ($C_Q < 2$ MHz), 10 kHz ($2 < C_Q < 3$ MHz), and 20 kHz ($C_Q > 3$ MHz).

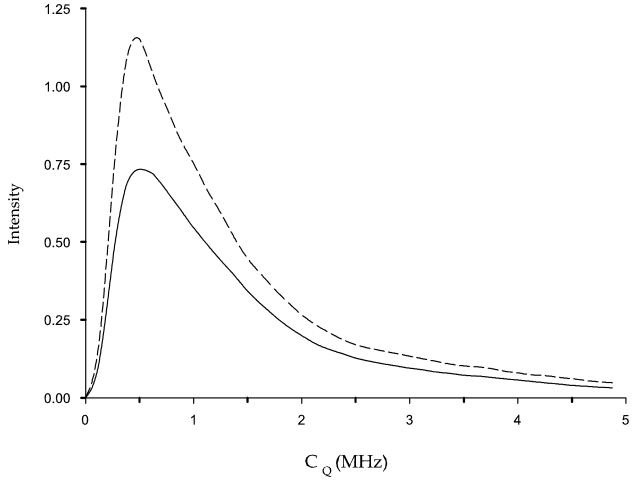

Fig. 3. $S = 3/2$: efficiency of the anti-echo pathway in full-anti-echo experiments without SPAM (continuous line: $0 \rightarrow +3 \rightarrow +1 \rightarrow -1$) and with $SPAM_{FAE}$ (dashed line: $0 \rightarrow +3 \rightarrow$ all $\rightarrow +1 \rightarrow -1$), with $B_1(\mathrm{HP}) = 100$ kHz. All other specifications as in Fig. 2.

requires taking into account the supplementary attenuation $e^{-2\tau/T'_2}$, which occurs on CT values with full-echo and full-anti-echo experiments. The evolution of the anti-echo amplitude versus C_Q is similar to that observed in Fig. 2. For all quadrupole interactions and all rf-fields, full-anti-echo efficiencies are approximately 80–90% larger than with z-filter. However, the gain obtained with SPAM for full-anti-echo sequence, Fig. 1C, is less than that observed for sequence in Fig. 1A (ca. 1.55 instead of 2), as evident from Fig. 3. This decrease of the SPAM gain is related to the use of an additional SP ($\approx 90^\circ_s$: Fig. 1C), which implies that the $+3Q \rightarrow +1Q$ transfer is performed indirectly in SPAM (through the 0,

$\pm 1Q$ levels), whereas it is performed directly in the full-anti-echo acquisition experiment performed without SPAM. For the pulse sequence in Fig. 1A, SPAM does not introduce any additional pulse being the same as the z-filter, and the global transfer is identical in the z-filter and SPAM sequences: $3Q \rightarrow 0Q/\text{all} \rightarrow -1Q$.

3.2. Echo sensitivity: experimental S/N ratios in 2D 3QMAS experiments

We here analyze the echo sensitivity and S/N ratios in 2D 3QMAS actual experiments. As noted earlier, while in z-filter experiments both echo and anti-echo pathways are collected simultaneously [12], they need to be collected in separate experiments in $\text{SPAM}_{\text{E/AE}}$ experiments. It may thus appear at first glance that the signal sensitivity gain of 2 in $\text{SPAM}_{\text{E/AE}}$ is counter-balanced by the fact that the corresponding experiment requires twice as many accumulations: half for the echo and half for the anti-echo. Actually, this is not the case, as experiments are recorded and treated in three different ways: hyper-complex (also known as States method) [29], or time proportional phase increments (TPPI) [30] methods for z-filter, and echo/anti-echo method [31] for $\text{SPAM}_{\text{E/AE}}$ experiments.

z-filter experiments lead to a single amplitude-modulated signal with respect to t_1. This leads to a frequency sign indiscrimination of the resonances with respect to the carrier frequency along the δ_1 dimension. This problem is solved by using the hyper-complex or TPPI acquisition and data treatment [5]. In the first case (STATES), this means recording another 2D data set obtained by changing the phase of HP_1 by 30° [29]. In the second case (TPPI), the phase of HP_1 is incremented linearly with t_1 in steps of 30° [30].

On the contrary, the $\text{SPAM}_{\text{E/AE}}$ method leads to the observation of two separated phase-modulated signals, one for the echo and one for the anti-echo pathways. This leads to the echo/anti-echo data treatment in which the real part of the final spectrum, which is the sum of the anti-echo and complex conjugate echo, is in pure absorption mode [31]. As the data from which the final spectrum is computed are phase-modulated with respect to t_1, frequency discrimination and phase corrections are achieved in the δ_1 dimension. Phase corrections in δ_2 need to be applied either before the sum is made, or by using a different combination of the echo and anti-echo spectra [31], or by generating a Hilbert transform of the real part [32].

In liquids, only isotropic interactions are observable. FIDs are thus maximum at $t_2 = 0$ simultaneously for both pathways, thus leading to an equal contribution to the spectrum from the echo and the anti-echo signals. It must also be reminded that to achieve the same resolution in δ_1, hyper-complex method records each t_1 increment twice, one with sine and one with cosine modulation [29]. Furthermore, TPPI doubles the total number of t_1 steps with respect to other methods [33]. Therefore, in liquids, the total number of indirect steps is the same for all experiments (hyper-complex, TPPI, echo/anti-echo) with the same δ_1 resolution.

Things are different in MQMAS, where echo and anti-echo signals have opposite refocusing slopes: $t_2 = \pm Rt_1$. Consequently, because of these opposite slopes, the signal is mainly related to the echo pathway and the number of indirect steps can be largely reduced in echo/anti-echo experiments by collecting fewer anti-echoes.

In Fig. 4, we demonstrate experimentally the signal enhancement obtained with SPAM method by observing the signal intensity of the first slice ($t_1 \approx 0$) of the ^{23}Na ($S = 3/2$) 3QMAS spectra of a well-crystallized $Na_4P_2O_7$ sample, which presents four different ^{23}Na species all resolved in the 2D 3QMAS spectrum at 11.7 T ($C_Q = 2.1$, 2.9, 2.3, and 3.2 MHz; $\eta_Q = 0.26$, 0.47, 0.70, and 0.59; and $\delta_{cs} = -1.7$, 3.1, -5.3, and -0.9 ppm) [34]. The experiments were carried out on a Bruker Avance 500 MHz spectrometer ($\nu_0 =$ 132.2 MHz) with rf-field amplitudes of 100 and 5 kHz for HP and SP, respectively. Fig. 4A is the result from a z-filter experiment, Fig. 4B is the result from $\text{SPAM}_{\text{E/AE}}$ sequence of Figs. 1A and 4C is the result from $\text{SPAM}_{\text{E/AE}}$ sequence of Fig. 1A where fewer

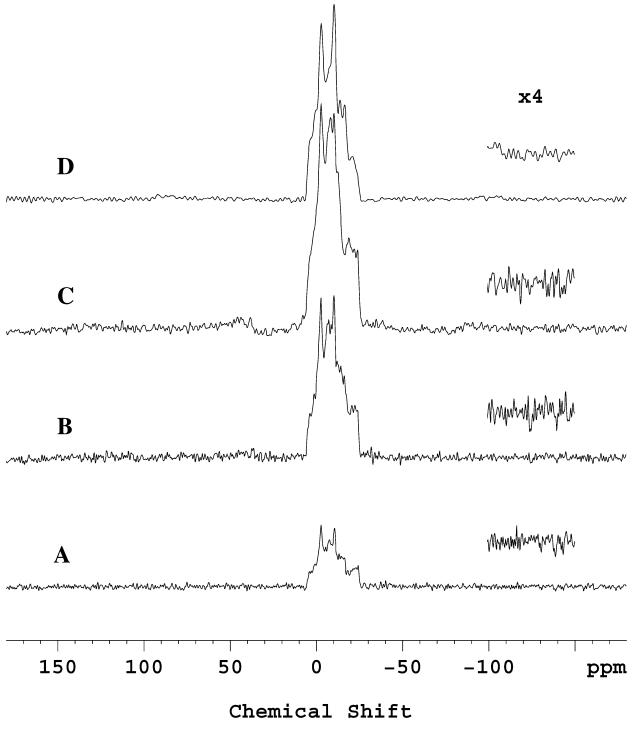

Fig. 4. $S = 3/2$: ^{23}Na 3QMAS anisotropic projections of 2D spectra of $Na_4P_2O_7$ with $\nu_0 = 132.2$ MHz, $\nu_R = 12.5$ kHz, acquisition time 636 s recorded with (A) z-filter (64R/64I, NS = 12), (B) $\text{SPAM}_{\text{E/AE}}$ (64E/64AE, NS = 12), (C) truncated $\text{SPAM}_{\text{E/AE}}$ (64E/12AE, NS = 20). (D) full-anti-echo spectrum observed with DFS (64E, NS = 24). On every projection, a vertical expansion of the noise is also displayed.

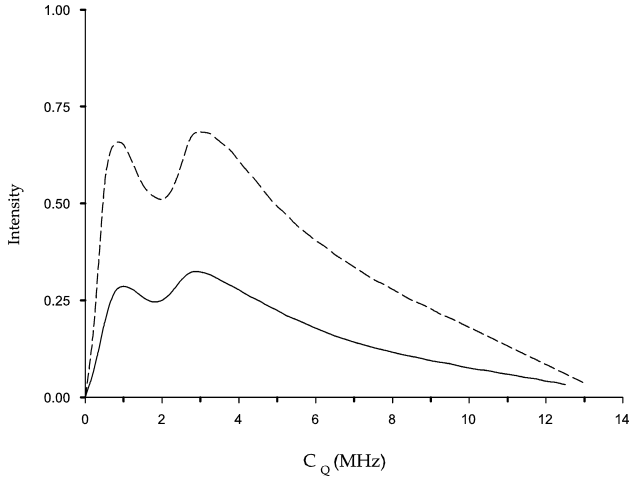

Fig. 5. $S = 5/2$: efficiency of the echo pathway in z-filter (continuous line: $0 \rightarrow +3 \rightarrow 0 \rightarrow -1$) and $\mathrm{SPAM_{E/AE}}$ (dashed line: $0 \rightarrow +3 \rightarrow$ all $\rightarrow -1$) experiments as a function of C_Q (0–15 MHz). $B_1(\mathrm{HP}) = 100$ kHz; $\eta_Q = 0$; $\nu_0 = 105$ MHz; $\nu_R = 10$ kHz ($C_Q < 9$ MHz), 15 kHz ($9 < C_Q < 12$ MHz), and 20 kHz ($C_Q > 12$ MHz); and $B_1(\mathrm{SP}) = 5$ kHz ($C_Q < 7$ MHz), 10 kHz ($7 < C_Q < 9$ MHz), and 20 kHz ($C_Q > 9$ MHz).

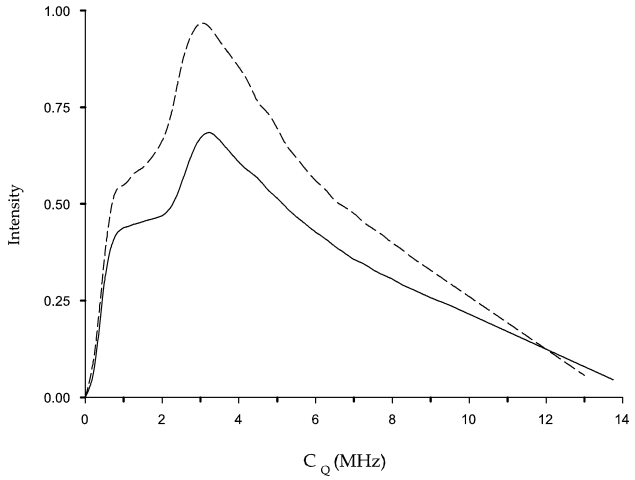

Fig. 6. $S = 5/2$: efficiency of the echo pathway in full-echo experiments without SPAM (continuous line: $0 \rightarrow +3 \rightarrow +1 \rightarrow -1$) and with $\mathrm{SPAM_{FE}}$ (dashed line: $0 \rightarrow +3 \rightarrow$ all $\rightarrow +1 \rightarrow -1$), with $B_1 = 100$ kHz. All other specifications as in Fig. 5.

anti-echoes are collected enabling more signal averaging, and Fig. 4D is the result from a PM full-anti-echo acquisition sequence employing DFS for signal enhancement. All the experiments were rotor-synchronized during t_1 ($\nu_R = 12.5$ kHz) and took the same amount of time. Practically, a proper S/N comparison requires the use of spectra recorded with identical experimental specifications: spinning speed, rf-fields, recycling delay, and total acquisition time.

By comparing Figs. 4A and B, the signal enhancement with $\mathrm{SPAM_{E/AE}}$ over the z-filter sequence is by a factor of 2.7. However, the noise is increased by $\sqrt{2}$ because echo and anti-echo signals must be acquired separately. This leads to a S/N gain of approximately 1.9. Echo/anti-echo data acquisition recorded without SPAM leads to the same signal intensity as for the z-filter acquisition, but with an increase of the noise level by $\sqrt{2}$ (not shown). The low noise level as well as the robustness of the experiment are the two main reasons that explain why the z-filter approach is at the moment the most frequently used method. Consequently, for the same experimental time, the S/N ratio can be increased by recording only a few FIDs for the anti-echo pathway and zero-filling all other FIDs to decrease the noise, the result of which is shown in Fig. 4C. Indeed, due to the negative ($-R$) slope of the anti-echo signal in the time domain, the contribution of the anti-echo pathway to the signal becomes negligible, if not non-existent, after a few t_1 steps, particularly for samples having short homogeneous T_2' time constants or presenting large distribution of surroundings. Therefore, long t_1 steps correspond to longer experimental times and to an increase in noise. The signal is then proportional to the number of scans (NS) accumulated for each t_1 increment and, thus, increases by a factor of 5/3 from Figs. 4B to C. Since the experimental time and hence the total number of scans are the same, the noise level remains identical in all echo/anti-echo spectra, whatever the number of recorded anti-echo t_1 slices be, as shown in Figs. 4B and C. An easy way to even double the signal and the S/N ratio with respect to Fig. 4B is to avoid recording any anti-echo FID, to use the first ($t_1 \approx 0$) FID of the echo-pathway for the anti-echo pathway, and to zero-fill all other anti-echo FIDs. With respect to Fig. 4C, we gain an additional factor of 1.2 for the signal and S/N ratio (not shown). However, this doubling of the S/N ratio is obtained at the expense of a small amount of additional dispersive signal. It must be kept in mind that even with the z-filter experiment, a dispersive signal is often observed, especially in case of sample with multiple sites with large differences in the quadrupolar strengths. Its amount increases with the second-order quadrupole interaction, with off-resonance irradiation, and also with decreasing rf-field. In SPAM experiments, the additional dispersive signal can be limited by equalizing transfer efficiencies from echo and anti-echo pathways, which may slightly differ. Dispersive signals are invisible on the projections, because their intensities integrated over F_1 or F_2 are null. However, they may limit the resolution of 2D spectra for well-crystallized compounds with narrow and close resonances.

For identical experimental time, full-anti-echo (or full-echo) acquisition PM sequences, which only use the echo-pathway (or anti-echo-pathway), can accumulate twice as many scans for each t_1 step than for the hyper-complex or TPPI z-filter and echo/anti-echo SPAM methods. When there is no additional transverse attenuation, this leads to a large S/N gain of PM methods with respect to z-filter methods. The signal obtained with full-

anti-echo acquisition PM sequence employing DFS shown in Fig. 4D is hence more than that obtained with z-filter sequence and $SPAM_{E/AE}$. However, the truncated $SPAM_{E/AE}$ method (Fig. 4C) is more efficient than the full-anti-echo acquisition PM pulse sequence. The noise level is higher in PM experiments by a factor of $\sqrt{2}$ with respect to z-filter experiments (Figs. 4A and D). It must be noticed that in this experiment, the delay $\tau = 5$ ms was much shorter than the transverse homogeneous relaxation time T'_2, therefore introducing no supplementary attenuation.

In conclusion, when comparing S/N ratios observed on spins-3/2 nuclei submitted to long T'_2 homogeneous relaxation times, best results are obtained either with a complete echo/anti-echo $SPAM_{E/AE}$ sequence shown in Fig. 1A or with a full-anti-echo acquisition sequence using FAM or DFS as conversion pulse (Figs. 4B and D). When used with no (or few) t_1 slices, 'truncated' echo/anti-echo $SPAM_{E/AE}$ sequence becomes more efficient than the full-anti-echo ones (Figs. 4C and D). This is especially true for samples where the extra transverse attenuation factor $e^{-2\tau/T'_2}$, which is close to 1 for $Na_4P_2O_7$, must also be taken into account for full-anti-echo methods.

4. Spins-5/2

4.1. Echo sensitivity: simulations

In this section, we analyze the intensity of the echo signal for spins-5/2 for the following experiments: z-filter, $SPAM_{E/AE}$, full-echo acquisition, and $SPAM_{FE}$.

We first compare the echo sensitivity of z-filter and $SPAM_{E/AE}$ experiments. The CT amplitude due to the echo pathway for both the experiments is plotted in Fig. 5 as a function of C_Q. The curves present two maxima and the amplitude of the echo signal observed with SPAM ($SPAM_{E/AE}$ sequence) is more than doubled.

We now compare the sensitivity in full-echo experiments with and without SPAM given in Fig. 6. The evolution of the echo amplitude versus C_Q is similar to that observed in Fig. 5. For all quadrupole interactions and all rf-fields, echo efficiencies of a full-echo acquisition experiment are approximately 80–90% larger than with z-filter. However, the gain obtained with SPAM for full-echo sequence, Fig. 1C, is less than that observed for sequence in Fig. 1A as evident from Figs. 5 and 6, and it even disappears for strong quadrupole interactions ($C_Q > 12$ MHz).

4.2. Echo sensitivity: experimental S/N ratios in 2D 3QMAS experiments

We have previously seen for spins-3/2 that full-anti-echo (and full-echo) acquisition methods are not always the best for S/N reasons, especially when taking into account the extra transverse attenuation factor. This is furthermore the case for spins-5/2 because the SPAM gain in full-echo experiments is always smaller than with spins-3/2 (Figs. 3 and 6). We have therefore focused our experimental efforts to record ^{27}Al z-filter and echo/anti-echo 3QMAS spectra of one test compound: $AlPO_4$-14. The sample used in this study was obtained by hydrothermal crystallization at 200 °C, during 24 h, from a gel of the following molar composition: 1 Al_2O_3 (pseudo-boehmite), 1 P_2O_5 (85% aqueous solution H_3PO_4), 2 isopropylamine (template), 100 H_2O, and 0.25 H_2SO_4. The initial pH of the gel was 3.5 [35]. This well-crystallized compound has four different aluminum species: two tetravalent, one pentavalent, and one hexa-coordinated ($C_Q = 1.74$, 4.08, 5.58, and 2.57 MHz; $\eta_Q = 0.63$, 0.82, 0.97, and 0.70; and $\delta_{cs} = 42.9$, 43.5, 27.1, and -1.3 ppm) [35]. ^{27}Al spectra were recorded on a Bruker Avance 500 spectrometer ($\nu_0 = 130.2$ MHz). Experiments were rotor-synchronized during t_1 ($\nu_R = 12.5$ kHz) and they used rf-field amplitudes of 150 and 5 kHz for HP and SP, respectively.

In the same way as for spins-3/2, we first verified (not shown) that the SPAM gain for the echo (or anti-echo) pathway is approximately 2 as predicted in Fig. 5. The performance efficiency of SPAM is tested by comparing the following sequences: z-filter, echo/anti-echo, $SPAM_{E/AE}$, and truncated $SPAM_{E/AE}$ with only 12 anti-echoes. The anisotropic projections obtained for hexa-coordinated aluminum with these sequences are shown in Figs. 7A–D, respectively.

As for spins-3/2, the z-filter and echo/anti-echo experiments gave identical signals with however a $\sqrt{2}$-noise increase for the echo/anti-echo method (Figs. 7A and B). $SPAM_{E/AE}$ method increases the signal as shown in Fig. 7C. In its truncated version of $SPAM_{E/AE}$, the gain for the signal is nearly 3, Fig. 7D, but simultaneously the noise also (echo/anti-echo acquisition) increased by a factor of $\sqrt{2}$, leading to a S/N gain of 2.1. Of course, the acquisition of only the echo (not shown) leads to a S/N gain of 2.5, but this implies some additional dispersive components. As said before, these dispersive parts are not observable on the projections, but they may slightly obscure the 2D analysis of well-crystallized compounds with close resonances, such as the tetravalent aluminum in $AlPO_4$-14 (Figs. 8A and B). To limit these dispersive parts, an easy way is to record a truncated $SPAM_{E/AE}$ spectrum using a few t_1 slices for the anti-echo pathway, and to zero-fill the other ones. In $AlPO_4$-14, using the first 10 t_1 slices was sufficient to cancel most dispersive parts (Fig. 8C). Introducing more t_1 slices did not change anything, as the corresponding signal was negligible. It must be noted that the dispersive signal is larger in Fig. 8C than in Fig. 8A. This is due to a slight difference in SPAM efficiency in between the echo and the anti-echo pathways recorded for identical HP_2 value.

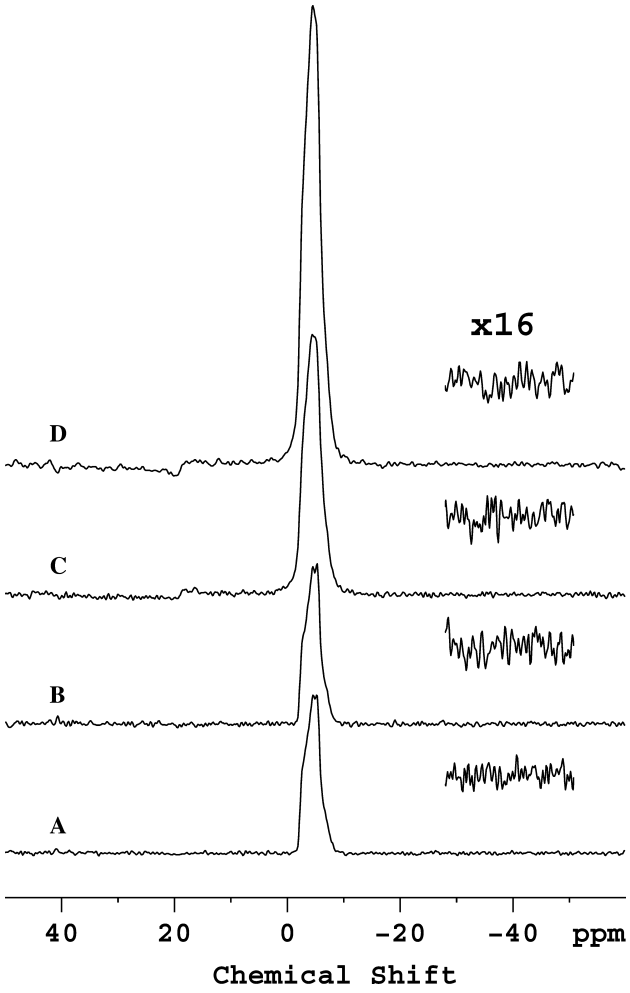

Fig. 7. $S = 5/2$: ^{27}Al 3QMAS anisotropic projection spectra corresponding to the hexa-coordinated part of $AlPO_4$-14 observed with (A) z-filter (64R/64I, NS = 12), (B) echo/anti-echo (64E/64AE, NS = 12), (C) complete $SPAM_{E/AE}$ (64E/64AE, NS = 12), and (D) truncated $SPAM_{E/AE}$ (64E/12AE, NS = 20). On every projection, a vertical expansion of the noise is also displayed.

Globally, the number of additional t_1 slices required to cancel the dispersive parts decreases with increasing R values and thus, with increasing spin values in 3QMAS ($R = 7/9$, 19/12, 101/45, and 91/36 for $S = 3/2$, 5/2, 7/2, and 9/2, respectively) [1,3]. This number also decreases with the broadness of the resonances, and it may be very limited with distributed samples (e.g., zeolites, ceramics, or glasses). In any case, as said previously, the first ($t_1 \approx 0$) FID of echo pathway can be used for anti-echo pathway. This slice introduces a positive component in the 2D spectrum, constant with respect to δ_1 and δ_{iso}, which slightly increases the signal. The other slices ($t_1 > 0$) are related to time signals modulated versus δ_1, not contributing to the anisotropic projection.

We have also recorded a 3QMAS spectrum with a full-echo acquisition sequence using a DFS conversion pulse (not shown). Noise level obtained was then identical to that observed with $SPAM_{E/AE}$, and $\sqrt{2}$ times higher with respect to z-filter. However, due to T_2' value comparable to the delay $\tau = 5$ ms, signal with DFS was only twice that observed with z-filter, and thus smaller than that observed with SPAM (Fig. 7D).

4.3. SPAM on distributed compounds

In the previous sections, we have demonstrated theoretically and experimentally on well-crystalline test samples, the advantages of using $SPAM_{E/AE}$ 3QMAS method, especially in its truncated version. To demonstrate practically this advantage on a distributed compound, we used the $SPAM_{E/AE}$ method to record ^{17}O 3QMAS spectra on an ^{17}O-enriched glass sample of composition $3Al_2O_3$–$48.5Na_2O$–$48.5P_2O_5$. The enriched sample was prepared by melting ^{17}O-enriched $50Na_2O$–$50P_2O_5$ [36] and non-enriched Al_2O_3 at 1000 °C for one hour. The absence of weight loss during the melting indicates that the actual sample composition is very close to the nominal one. The ^{17}O enrichment level is estimated to be 20%. We used a Bruker AVANCE 400 spectrometer, with a spinning speed of $\nu_R = 10$ kHz, and an rf-field of approximately 150 and 10 kHz for the HP and SP, respectively. According to previous X-ray photoelectron spectroscopy (XPS) at O1s core level

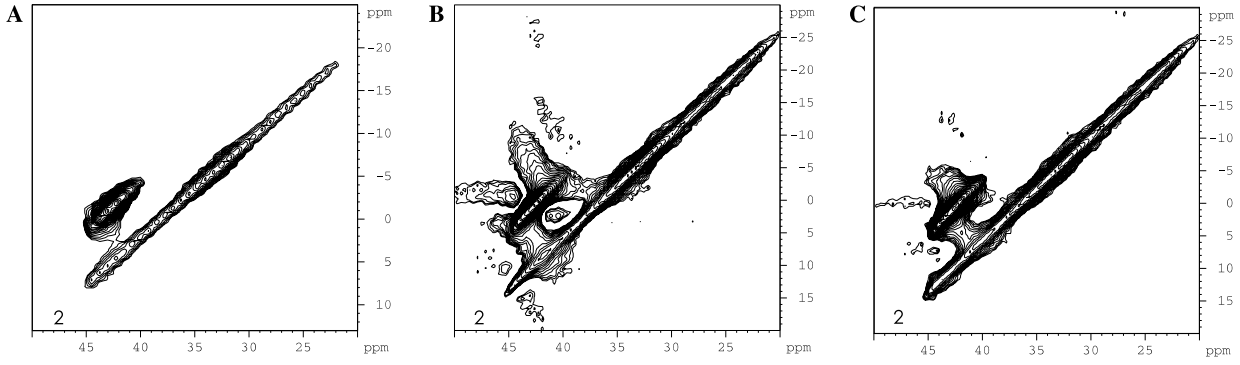

Fig. 8. $S = 5/2$: ^{27}Al 3QMAS 2D spectra of the tetrahedral part of $AlPO_4$-14 observed with: (A) z-filter (128 R/128I), (B) only echo $SPAM_{E/AE}$ without any anti-echo slice (128E/0AE), and (C) truncated $SPAM_{E/AE}$ (128E/10AE).

[37], this sample contains three types of oxygen sites: one site is located between two phosphorus atoms (POP) and is involved in covalent phosphorus–oxygen bonds. It is the bridging oxygen. The second type of oxygen is involved in PO···Na groups, and the O···Na bond has an ionic character. This oxygen is a non-bridging oxygen. The third type of oxygen is linked to phosphorus and aluminum (PO···Al) through bonds with a mixed iono-covalent character. It has been shown that in oxide materials, the ^{17}O quadrupolar coupling constant is proportional to the covalent character of M–O–M′ bonds (here M,M′ = Na, P, and Al) [38]. With this model, we were able to assign, in sodium phosphate glasses [36], non-bridging oxygens (PO···Na) to moderate quadrupolar coupling constants (4–5 MHz) and bridging oxygen (POP) to a larger quadrupolar coupling constant (typically 7 MHz). Bridging oxygens, with such a large quadrupolar coupling constant, require very high magnetic fields to be detected in the 3QMAS spectrum. Therefore, they are barely visible at the magnetic field we used (9.4 T), probably also due to the weak ^{17}O enrichment. The 3QMAS spectra of the $3Al_2O_3$–$48.5Na_2O$–$48.5P_2O_5$ glass are thus presented only in the non-bridging oxygen region. This sample is a glass, and the broad resonances thus represent distributed surroundings. Two sites are clearly visible on the isotropic projection, shown in Fig. 9, which can be assigned to PO···Na (≈100 ppm) and PO···Al (≈120 ppm) sites as bridging POP oxygen is not detected. Considering the glass composition, the most intense resonance is attributed to oxygens in PO···Na, and the least intense to oxygens in PO···Al sites. We notice that PO···Al oxygen sites appear in the non-bridging region of the 3QMAS spectrum, which may seem surprising since aluminophosphate compounds generally exhibit bonds with large covalent POAl character. However, in sodium aluminophosphate glasses, ^{27}Al MAS-NMR has shown that most of Al^{3+} are in octahedral coordination [37]. The aluminum–oxygen bonds have thus a large ionic character in such materials leading to moderate ^{17}O C_Q value for PO···Al. Despite the fact that bridging oxygens were not detected, the 3QMAS spectrum provides the first direct structural evidence for the presence of distinct PO···Na and PO···Al sites in glasses, as they are not resolved on XPS spectra [37]. From the 2D spectra, we have determined averaged values of $P_Q = C_Q(1+\eta_Q^2/3)^{1/2} \approx 4.3$ and 5 MHz, with $\delta_{cs} \approx 78$ and 89 ppm for PO···Na and PO···Al, respectively. We will now use this sample to show the interest of using SPAM method for distributed samples.

Fig. 9 shows the isotropic sheared projection of 2D 3QMAS spectra obtained with hyper-complex z-filter (A), truncated $SPAM_{E/AE}$ (B), and only echo $SPAM_{E/AE}$ with the anti-echo FIDs being zero-filled (C). In the latter case, even without recording any t_1 slice, the dispersive parts are nearly undetectable on the $SPAM_{E/AE}$ spectrum, due to the broadness of the resonance. The S/N enhancement is obvious on the isotropic projections and corresponds approximately to a factor of 2.8–3.

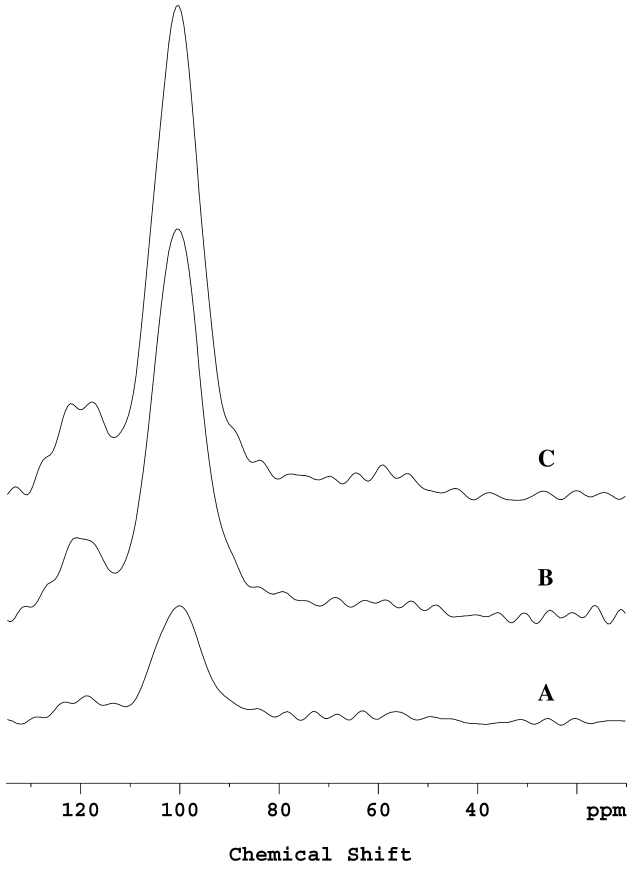

Fig. 9. $S = 5/2$: ^{17}O 3QMAS isotropic projection of $3Al_2O_3$–$48.5Na_2O$–$48.5P_2O_5$ glass, recorded with same total experimental time. (A) z-filter (32 R/32I, NS = 240), (B) truncated $SPAM_{E/AE}$ (32E/8AE, NS = 384), and (C) only echo $SPAM_{E/AE}$ (32E/0AE, NS = 480).

5. Discussion

The SPAM principle (adding constructively several pathways instead of using a single one) is a simple but an efficient idea. It largely increases the S/N ratio of various MQMAS experiments, especially in the case of distributed samples where no or very few anti-echo t_1 slices are necessary. It presents the great advantage of being robust and being for the users completely identical to the previous z-filter method (two HPs followed by a $90°_s$ pulse), as only the phase cycling differs. This means that it requires very little experimental optimization, and thus can be used on samples with a low sensitivity (e.g., low γ-nuclei). Indeed, the SPAM method requires only optimizing the two HP lengths as in z-filter method, the rf amplitude then being set at its maximum. SPAM MQMAS also has the great advantage of not being tech-

Table 1
Comparison of Signal (S), Noise level (N), and S/N ratio that can be obtained in various MQMAS methods

	S	N	S/N
z-filter classical (States/TPPI)	1	1	1
z-filter multiplex (States/TPPI)	≈ 3	$\sqrt{3}$	$\approx\sqrt{3}$
E/AE	1	$\sqrt{2}$	$1/\sqrt{2}$
$SPAM_{E/AE}$ complete	≈ 2	$\sqrt{2}$	$\approx\sqrt{2}$
$SPAM_{E/AE}$ truncated	≈ 4	$\sqrt{2}$	$\approx 2\sqrt{2}$
Full-echo	$\approx 2e^{-2\tau/T_2'}$	$\sqrt{2}$	$\approx \sqrt{2}e^{-2\tau/T_2'}$
Full-echo SPAM	$\approx 3e^{-2\tau/T_2'}$	$\sqrt{2}$	$\approx 2e^{-2\tau/T_2'}$

nically demanding, and thus, being usable on any spectrometer. In Table 1, we compare with respect to the z-filter: signals, noise levels, and S/N ratios that can be obtained with various CW MQMAS methods. We also introduce values for the recently proposed multiplex method applied to MQMAS [25]. This method is a hyper-complex (or TPPI) z-filter type of experiment, and at the end the signal and noise level are multiplied by approximately 3 and $\sqrt{3}$, respectively, with respect to the z-filter method.

It must be noted that sensitivities with respect to spinning speed in MQMAS sequences with or without SPAM are identical. This means that efficiencies of $0Q \leftrightarrow \pm 3Q$ transfers decrease with fast spinning speed, especially when using weak rf-fields for HPs [28]. It must also be noted that all MQMAS methods (with or without SPAM conversion pulse) give non-quantitative experimental results due to transfers to or from multiple-quantum levels. The only way to quantify the results is by using appropriate software taking into account all sample and experimental specifications [39]. The main advantage of the $SPAM_{E/AE}$ method, over z-filter, results from the fact only few anti-echo t_1 steps need to be recorded without affecting the broad 2D resonance lineshapes in distributed samples. A question immediately arises: how does one know where to get away with truncating the SPAM anti-echoes without recording before the 3QMAS or STMAS spectrum? One way is to record first all echo-FIDs, and then to record anti-echo FIDs with increasing t_1 values up to the time where there is no detectable signal. Of course, this number decreases largely when going from well-crystallized to distributed samples. As an example, on glasses it has been our experience that no, or less than five, anti-echo t_1 slices are only necessary to obtain 2D $SPAM_{E/AE}$ spectra without any detectable dispersive signals. This may be the same on most of distributed samples, such as ceramics or dealuminated zeolites. It must be noted that a large majority of researchers using solid-state NMR, especially in industries, are most of the time recording MQMAS spectra on the same types of samples and on the same few different nuclei with half-integer spin. In this case, after a few tests these researchers will know in advance the number of anti-echo steps that must be recorded, according to the sample and nuclei they will analyze.

The SPAM principle can easily be applied to several other 2D high-resolution methods, such as 5QMAS [40] or double-quantum filtered STMAS [41]. It can be used for hetero-nuclei distance measurement under high-resolution with methods such as CP-MQMAS/STMAS [42], MQ-CP-MQMAS [43], TEDOR-MQMAS/STMAS [5], PRESTO-MQMAS/STMAS [44], and MQ/ST-REDOR [45]. It can also be used in high-resolution HETCOR experiments involving quadrupolar nuclei with half-integer spin, such as 2D MQ-HETCOR [46], 2D MQ-J-HETCOR [47,48], or 3D MQ-J-HMQC [49]. These three HETCOR-type experiments are different from MQMAS because only the echo signal is then required, and because we compare efficiencies obtained using different pathways: $0 \rightarrow +3 \rightarrow +1$ with respect to $0 \rightarrow +3 \rightarrow \text{all} \rightarrow +1$ (if $S = 3/2$: Fig. 3) or $0 \rightarrow -3 \rightarrow +1$ with respect to $0 \rightarrow -3 \rightarrow \text{all} \rightarrow +1$ (if $S > 3/2$). In principle, the SPAM concept can be extended to other types of conversion pulses (RIACT, DFS, and FAM). However, it must be kept in mind that to be efficient with SPAM, these pulses must transfer approximately the same amount of magnetization on the three 0, ± 1 coherence levels. Finally, the SPAM principle can be combined with other solid-state NMR tools for further S/N enhancement, such as initial pre-saturation [15,17,23], a posteriori echo CPMG recycling [21], or rotor-synchronization [24].

Acknowledgments

Authors (J.P.A., L.D., and L.M.) thank Region Nord/Pas de Calais and Europe (FEDER) for funding. They also thank Dr. P.K. Madhu for largely improving the manuscript and for the long discussions they had with him.

References

[1] L. Frydman, J.S. Harwood, Isotropic spectra of half-integer quadrupolar spins from bidimensional magic-angle-spinning NMR, J. Am. Chem. Soc. 117 (1995) 5367–5368.
[2] Z.H. Gan, Isotropic NMR spectra of half-integer quadrupolar nuclei using satellite transitions and magic-angle-spinning, J. Am. Chem. Soc. 122 (2000) 3242–3243.
[3] J.P. Amoureux, High-resolution solid-state NMR for spin 3/2 and 9/2: the multiple-quantum transitions method, Solid-State NMR. 2 (1993) 83–88.
[4] J.P. Amoureux, C. Fernandez, Triple, quintuple and higher-order multiple quantum MAS NMR of quadrupolar nuclei, Solid-State NMR. 10 (1998) 211–223; Solid-State NMR 16 (2000) 339–343.
[5] J.P. Amoureux, M. Pruski, Advances in MQMAS NMR, in: Encyclopedia of NMR, second ed., vol. 9, 2002, pp. 54–90.
[6] L. Frydman, Fundamental of MQMAS NMR on half-integer quadrupolar nuclei, in: Encyclopedia of NMR, second ed., vol. 9, 2002, pp. 262–274.

[7] S.E. Ashbrook, S. Antonijevic, A.J. Berry, S. Wimperis, Motional broadening: an important distinction between multiple-quantum and satellite-transition MAS NMR of quadrupolar nuclei, Chem. Phys. Lett. 364 (2002) 634–642.
[8] J.P. Amoureux, C. Huguenard, F. Engelke, F. Taulelle, Unified representation of MQMAS and STMAS NMR of half-integer quadrupolar nuclei, Chem. Phys. Lett. 356 (2002) 497–504.
[9] A. Medek, J.S. Harwood, L. Frydman, Multiple-quantum magic-angle spinning NMR: a new method for the study of quadrupolar nuclei in solids, J. Am. Chem. Soc. 117 (1995) 12779–12787.
[10] G. Wu, D. Rovnyak, B. Sun, R.G. Griffin, High-resolution multiple-quantum MAS NMR spectroscopy of half-integer quadrupolar nuclei, Chem. Phys. Lett. 249 (1996) 210–217.
[11] J.P. Amoureux, C. Fernandez, L. Frydman, Optimized multiple-quantum magic-angle spinning NMR experiments on half-integer quadrupoles, Chem. Phys. Lett. 295 (1996) 347–355.
[12] J.P. Amoureux, C. Fernandez, S. Steuernagel, Z-filtering in MQMAS NMR, J. Magn. Reson. A123 (1996) 116–118.
[13] D. Massiot, B. Touzo, D. Trumeau, J.P. Coutures, J. Virlet, P. Florian, P.J. Grandinetti, Two-dimensional magic-angle spinning isotropic reconstruction sequences for quadrupolar nuclei, Solid State NMR. 6 (1996) 73–83.
[14] S.P. Brown, S. Wimperis, Two-dimensional multiple-quantum MAS NMR of quadrupolar nuclei, acquisition of the whole echo, J. Magn. Reson. 124 (1997) 279–285.
[15] P.K. Madhu, O.G. Johannessen, K.J. Pike, R. Dupree, M.E. Smith, M.H. Levitt, Application of amplitude-modulated radio-frequency fields to the magic-angle spinning of spin 7/2 nuclei, J. Magn. Reson. 163 (2003) 310–317.
[16] G. Wu, D. Rovnyak, R.G. Griffin, Quantitative multiple-quantum magic-angle-spinning NMR spectroscopy of quadrupolar nuclei in solids, J. Am. Chem. Soc. 117 (1996) 9326–9332.
[17] P.K. Madhu, A. Goldbourt, L. Frydman, S. Vega, Sensitivity enhancement of the MQMAS NMR experiment by fast amplitude modulation of the pulses, Chem. Phys. Lett. 307 (1999) 41–47.
[18] A.P.M. Kentgens, R. Verhagen, Advantage of double frequency sweeps in static, MAS and MQMAS NMR of spin $I = 3/2$, Chem. Phys. Lett. 300 (1999) 435–443.
[19] T. Vosegaard, P. Florian, D. Massiot, P.J. Grandinetti, Multiple-quantum magic-angle-spinning using rotary resonance excitation, J. Chem. Phys. 114 (2001) 4618–4624.
[20] G. Mali, G. Fink, F. Taulelle, Double-quantum homonuclear correlation MAS NMR spectroscopy of dipolar-coupled spin-5/2 nuclei, J. Chem. Phys. 120-6 (2004) 2835–2845.
[21] T. Vosegaard, F.H. Larsen, H.J. Jakobsen, P.D. Ellis, N.C. Nielsen, Sensitivity-enhanced multiple-quantum MAS NMR of half-integer quadrupolar nuclei, J. Am. Chem. Soc. 119 (10) (1997) 9055–9056.
[22] R. Lefort, J.W. Wiench, M. Pruski, J.P. Amoureux, Optimization of data acquisition and processing in Carr–Purcell–Meiboom–Gill multiple-quantum MAS NMR, J. Chem. Phys. 116 (4) (2002) 2493–2501.
[23] Z. Yao, H.T. Kwak, D. Sakellariou, L. Emsley, P.J. Grandinetti, Sensitivity enhancement of the central transition of quadrupolar nuclei under MAS, Chem. Phys. Lett. 327 (2000) 85–90.
[24] D. Massiot, Sensitivity and lineshape improvements of MQMAS by rotor-synchronization, J. Magn. Reson. A122 (1996) 240–244.
[25] Z. Gan, H.T. Kwak, Enhancing MQMAS sensitivity using signals from multiple coherence transfer pathways, J. Magn. Reson. 168 (2004) 346–351.
[26] N. Ivchenko, C.E. Hughes, M.H. Levitt, Multiplex phase cycling, J. Magn. Reson. 160 (2003) 52–58.
[27] R.R. Ernst, G. Bodenhausen, A. Wokaun, Principles of Nuclear Magnetic Resonance in One and Two Dimensions, Clarendon, Oxford, 1987.
[28] J.P. Amoureux, M. Pruski, D.P. Lang, C. Fernandez, The effect of rf-power and spinning speed on MQMAS NMR, J. Magn. Reson. 131 (1998) 170–175.
[29] D.J. States, R.A. Haberkorn, D.J. Ruben, J. Magn. Reson. 48 (1982) 256.
[30] A. Bax, R. Freeman, S.P. Kempsell, J. Magn. Reson. 41 (1980) 349.
[31] A.L. Davis, J. Keeler, E.D. Laue, D. Moskau, Experiments for recording pure-absorption heteronuclear correlation spectra using pulse field gradients, J. Magn. Reson. 98 (1992) 207–216.
[32] R.M. Bracewell, The Fourier Transform and its Applications, second ed., Mc Graw-Hill, New York, 1978.
[33] D. Marion, K. Wüthrich, Biochem. Biophys. Res. Commun. 113 (1983) 967.
[34] G. Engelhard, A.P.M. Kentgens, H. Koller, A. Samoson, Strategies for extracting NMR parameters from ^{23}Na MAS, DOR and MQMAS spectra. A case study for $Na_4P_2O_7$, Solid State NMR. 15 (1999) 171–180.
[35] C. Fernandez, J.P. Amoureux, J.M. Chezeau, L. Delmotte, H. Kessler, ^{27}Al MAS NMR characterization of $AlPO_4$-14 enhanced resolution and information by MQMAS, Microporous Mater. 6 (1996) 331–340.
[36] M. Zeyer, L. Montagne, V. Kostoj, G. Palavit, C. Jaeger, ^{17}O nuclear magnetic resonance of Na_2O–P_2O_5 glasses, J. Non. Cryst. Solids. 311 (2002) 223–232.
[37] R.K. Brow, Structure of sodium alumino-phosphate glass, J. Am. Cer. Soc. 76 (4) (1993) 919–926.
[38] S. Schramm, E. Oldfield, High-resolution oxygen-17 NMR of solids, J. Am. Chem. Soc. 106 (1984) 2502–2506.
[39] C. Fernandez, L. Delevoye, J.P. Amoureux, D.P. Lang, M. Pruski, ^{27}Al{^{1}H} cross-polarization triple-quantum magic-angle spinning NMR, J. Am. Chem. Soc. 129 (1997) 6858–6862.
[40] C. Fernandez, J.P. Amoureux, 2D multiple-quantum MAS NMR spectroscopy of ^{27}Al in alumino-phosphate molecular sieves, Chem. Phys. Lett. 242 (1995) 449–454.
[41] H.T. Kwak, Z. Gan, Double-quantum filtered STMAS, J. Magn. Reson. 164 (2003) 369–372.
[42] M. Pruski, D. Lang, C. Fernandez, J.P. Amoureux, Multiple quantum MAS-NMR with cross polarization : spectral editing of high resolution spectra of quadrupolar nuclei, Solid State NMR. 7 (4) (1997) 327–331.
[43] S.E. Ashbrook, S.P. Brown, S. Wimperis, Multiple-quantum cross-polarization in MAS NMR of quadrupolar nuclei, Chem. Phys. Lett. 288 (1998) 509–517.
[44] X. Zhao, W. Hoffbauer, J.S.A.D. Günne, M.H. Levitt, Heteronuclear transfer by symmetry-based recoupling sequences in solid-state NMR, Solid State NMR. (2004).
[45] C. Fernandez, D. Lang, J.P. Amoureux, M. Pruski, Measurement of heteronuclear dipolar interactions between quadrupolar and spin 1/2 nuclei in solids by multiple quantum REDOR-NMR, J. Am. Chem. Soc. 120 (11) (1998) 2672–2673.
[46] C. Fernandez, C. Morais, J. Rocha, M. Pruski, High-resolution heteronuclear correlation spectra between ^{31}P and ^{27}Al in microporous aluminophosphates, Solid State NMR. 21 (2002) 61–70.
[47] J.W. Wiench, M. Pruski, Probing through-bond connectivities with MQMAS NMR, Solid. State. NMR. 26 (2004) 51–55.
[48] J.P. Amoureux, J.W. Wiench, J. Trebosc, M. Pruski, J. Frye, Enhancing the sensitivity of MQ-J-HETCOR experiments (to be submitted).
[49] D. Massiot, Heteronuclear correlations involving quadrupolar nuclei, a through bond approach using *J* couplings, poster 278, in: 45th Rocky-Mountain Conference on Analytical Chemistry, July 27–31, 2003.